Research Article | Vol. 14, No. 12 / 1 Dec 2023 / Biomedical Optics Express 6222
Biomedical Optics EXPRESS

Descanned fast light targeting (deFLiT) two-photon optogenetics

CECILE TELLIEZ,[1] VINCENT DE SARS,[1] VALENTINA EMILIANI,[1,2] AND EMILIANO RONZITTI[1,3]

[1] Sorbonne Université, INSERM, CNRS, Institut de la Vision, 75012 Paris, France
[2] valentina.emiliani@inserm.fr
[3] emiliano.ronzitti@inserm.fr

Abstract: Two-photon light-targeting optogenetics allows controlling selected subsets of neurons with near single-cell resolution and high temporal precision. To push forward this approach, we recently proposed a fast light-targeting strategy (FLiT) to rapidly scan multiple holograms tiled on a spatial light modulator (SLM). This allowed generating sub-ms timely-controlled switch of light patterns enabling to reduce the power budget for multi-target excitation and increase the temporal precision for relative spike tuning in a circuit. Here, we modified the optical design of FLiT by including a de-scan unit (deFLiT) to keep the holographic illumination centered at the middle of the objective pupil independently of the position of the tiled hologram on the SLM. This enables enlarging the number of usable holograms and reaching extended on-axis excitation volumes, and therefore increasing even further the power gain and temporal precision of conventional FLiT.

1. Introduction

The emergence of genetically-encoded light-driven actuators [1–3] has revolutionized neurobiology providing a unique tool to manipulate the activity of neurons with light. In optics, that has spurred the development of several strategies which shape light and activate targeted sets of neurons [4–7], thereby enabling fine-scale control of neural microcircuits [8–12] as mapping connectivity functionally [13] or linking activity patterns to behavior [14–17].

Optogenetic light-targeting is generally obtained by shaping the wavefront of a two-photon (2P) excitation beam, typically with computer-generated phase holograms (CGH) displayed on liquid-crystal spatial light modulators (LC-SLM) [18]. Few different designs have been proposed each with its advantages and limitations. The 2P laser can be holographically split in multiple diffraction-limited spots, which are then spirally scanned on the targeted cells [8,19,20]. Alternatively, the 2P beam can be patterned in cell-sized spots, thereby maximizing the number of opsins excited per cell [10] and facilitating precisely timed spiking events in the neurons [11,12,21]. In this last configuration, a multi-step phase modulation is typically used [22–24] (Fig. 1(a)). First, the beam is tailored in a circular spot either by using a collimated low-NA gaussian beam [11,23] or providing a light-shaping phase modulation [12,21]. Second, the spot is projected on a diffracting grating which disperses the beam and provides for temporal focusing [25], thus axial confinement of the 2P excitation [25,26]. Finally, the spot is spatially multiplexed by displaying a CGH on a SLM that encodes the 3D coordinates of the targets [22].

It is critical to note that, for low-NA gaussian beams (and also for generalized phase contrast beams) [10,23,24], the beam diffracted by the grating results in a line focus beam of dispersed colors on the SLM, which underfills the multiplexing SLM display in the direction orthogonal to the dispersion (Fig. 1(a), insets). Taking advantage of this line focused illumination, we recently proposed an optical system for fast light-targeting (FLiT) where the SLM is parallelly addressed with H distinct tiled holograms and an upstream galvanometric mirror is used to

#499445 https://doi.org/10.1364/BOE.499445
Journal © 2023 Received 30 Jun 2023; revised 11 Sep 2023; accepted 25 Sep 2023; published 8 Nov 2023

Biomedical Optics EXPRESS

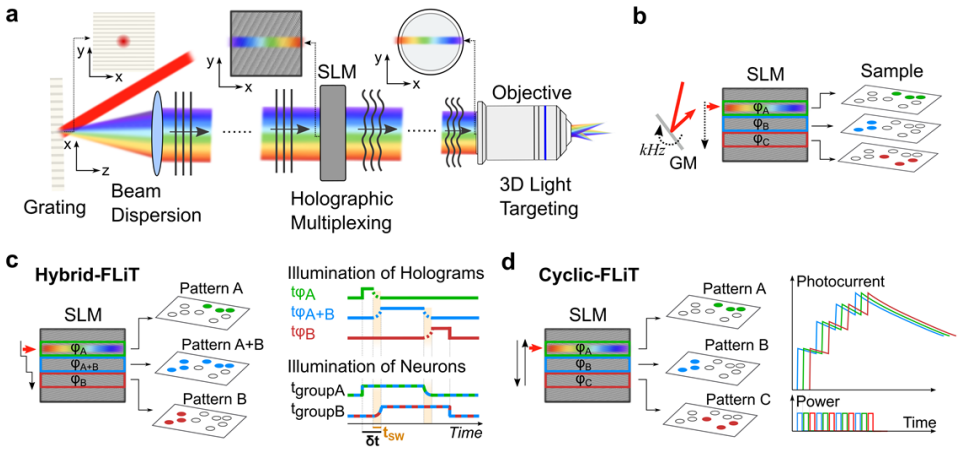

Fig. 1. Holographic fast-light targeting (FLiT). (a) Schematics of 3D holographic multiplexing. A 2P gaussian spot (red beam) is dispersed by a grating in a spatially-chirped beam and directed to a Spatial Light Modulator (SLM) which multiplexes the gaussian spot on different x,y,z locations in the sample plane. Top insets indicate the xy beam distribution on the grating, on the display of the SLM and on the objective back aperture (OBA). **(b)** Schematics of FLiT. A galvanometric mirror (GM) switches between holograms tiled on the SLM, each encoding different light-patterns. **(c)** Conceptual scheme of *hybrid*-FLiT. Holograms φ_A and φ_B on the SLM encode for group of spots A and B, respectively; hologram φ_{A+B} encodes for a pattern including group A and group B. By switching the beam vertically across the three holograms with predetermined dwell-times ($t_{\varphi A}$, $t_{\varphi B}$, $t_{\varphi A+B}$) and illumination powers ($P_{\varphi A}$, $P_{\varphi B}$, $P_{\varphi A+B} = P_{\varphi A} + P_{\varphi B}$) per each mask, it is possible to set an arbitrary δt delay ($\delta t = t_{\varphi A} + t_{SW}$) of activation between the two groups of spots which are illuminated for total durations $t_{groupA} = t_{\varphi A} + t_{\varphi A+B}$ and $t_{groupB} = t_{\varphi B} + t_{\varphi A+B}$. t_{SW} indicates the switching time to reposition the laser beam from one hologram to the next. **(d)** Conceptual scheme of *cyclic*-FLiT. Different holograms on the SLM encode for different multi-cell patterns. The illumination beam is cyclically scanned across the holograms and a cyclic photoactivation process is enabled on the different light patterns in parallel.

rapidly switch the line focus beam among them (Fig. 1(b)) [27]. This enabled to demonstrate two new illumination protocols for optogenetic multi target stimulations. A first one, that we termed hybrid-FLiT (Fig. 1(c)), enables tuning the relative firing time of $\frac{H+1}{2}$ groups of cells with µs-range temporal precision. The second one, that we termed, cyclic-FLiT (Fig. 1(d)), enables multi target stimulation using $\sqrt{H}$- to H-times less power than what used in conventional holography and so to proportionally scale up the number of achievable targets and/or reduce sample heating.

In both configurations, the tilt and drop of power induced by the objective back aperture to the off-axis holograms (i.e., situated at the edges of the SLM and at the side of the objective back aperture), have limited the usable holograms to those close to the pupil center, corresponding to ~50% of the total SLM vertical size and have generated tilting in the volumes of excitation. To overcome these limitations, we here propose an alternative scheme incorporating a de-scan unit which allows rapidly switching among different holograms while steadily maintaining the illumination beam in the middle of the illumination objective pupil. We demonstrated that this configuration enables to use the entire SLM vertical size and reach uniform on-axis volumes of excitation.

Biomedical Optics EXPRESS

2. Materials and methods

2.1. Optical system

The optical system (Fig. 2(a)) comprised two optical paths for descanned FLiT (deFLiT, Fig. 2(a), grey area), and conventional FLiT (Fig. 2(a), blue area) configuration. The system was supplied by a Ti:Sapphire laser tuned at 920 nm (Chameleon Ultra II, Coherent, repetition rate 80 MHz, pulse width 100 fs, 1.5W max output power). Power was controlled by an acousto-optic modulator (AOM) for fast intensity modulation (AA Opto-Electronic, France). The laser beam was initially

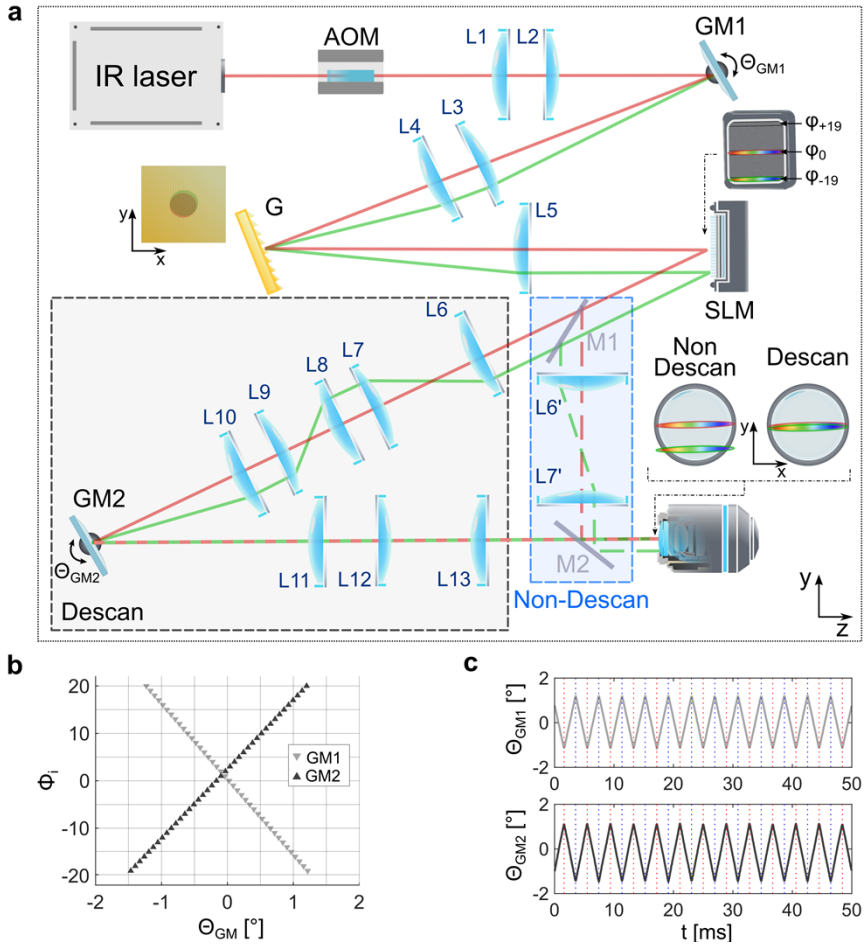

Fig. 2. Descanned holographic fast-light targeting (deFLiT) (a) Scheme of the experimental setup of deFLiT. Red and green beams represent the light pathway of a beam illuminating holograms on the edges (green) or in the middle (red) of the SLM. Blue and gray outlines show the non-descanned and the descanned pathway, respectively. Insets indicate xy beam distribution on the SLM (green and red beams are spatially shifted), on the grating and on the OBA (green/red beams overlapping in descanned and are separated in non-descanned mode). AOM: Acousto-Optic Modulator; L: Lens; M: movable Mirror; GM: Galvanometric Mirror; SLM: Spatial Light Modulator; G: Grating. **(b)** Tilting angle of the galvanometric mirrors GM1 and GM2 depending on the tiled hologram addressed on the SLM. SLM was subdivided in 39 equal tiled horizontal holograms. **(c)** Synchronized time courses of the tilting angle for GM1 and GM2 when scanning the full SLM extent in a cyclic manner.

Biomedical Optics EXPRESS

demagnified with a 4f telescope (f1 = 500 mm, f2 = 300 mm) and collimated onto a pair of galvanometric mirrors (GM1) (3 mm aperture, protected silver coating, 6215 H series; Cambridge Technology). GM1 plane was conjugated by means of a magnifying telescope (f3 = 200 mm, f4 = 400 mm) to a reflective dispersion grating of 800 lines/mm used to temporally focus [25,26] the pulse of the beam. The spatially-chirped beam diffracted by the grating was focused by a lens (f5 = 500 mm) on a reconfigurable liquid-crystal-silicon spatial light modulator LC-SLM (LCOS-SLM X10468-07, Hamamatsu Photonics, resolution 800 × 600 pixels, 20μm pixel size), located in the Fourier plane of the diffraction grating. In the deFLiT path (Fig. 2(a), grey area: descanned path), the beam reflected by the SLM was Fourier Transformed by a lens (f6 = 300 mm) and then relayed (f7 = 500 mm, f8 = 250 mm; f9 = 400 mm, f10 = 150 mm) onto a second pair of galvanometric mirrors (GM2) (3 mm aperture, protected silver coating, 6215 H series; Cambridge Technology). The beam reflected by GM2 was inversely Fourier transformed (f11 = 100 mm) and imaged at the objective back aperture (OBA) of a microscope objective (Olympus LUMPlanFL 40XW NA 0.8) through a final telescope (f12 = 1000 mm, f13 = 500 mm) to match the size of the objective back aperture. In the non-descanned path (Fig. 2(a), blue area), the LC-SLM was directly conjugated to the OBA with a single telescope (f6' = 750 mm, f7' = 750 mm). Two removable mirrors (M1, M2) allowed switching between the two paths. Lenses between the LC-SLM and the OBA in both FLiT and deFLiT paths were chosen as to fill the OBA with the chirped illumination in order to maximize the effect of temporal focusing on the axial resolution. The total de-magnification of the LC-SLM size at the OBA for FLiT and deFLiT was ~ 1 and ~ 0.9, respectively.

Following a previously validated computation scheme [27], the LC-SLM was addressed with multiple independent holograms, vertically aligned along the y-direction (i.e., the direction perpendicular to the grating's dispersion). In particular, the SLM was subdivided in up to 39 holograms φ_i, with i = 0 and i = ±19 corresponding to the hologram located in the middle and at the edges of the SLM display, respectively (1 hologram = 600 × 20 pixels) (Fig. 2(a), inset). Each hologram was encoded to generate arbitrary 2D or 3D patterns of gaussian spots in the sample plane by using a weighted Gerchberg and Saxton algorithm [28]. The zero order was physically blocked in the image plane of the lens after the SLM. After dispersion through the grating for temporal focusing, the spatially-chirped beam was scanned through the multiple holograms by controlling the tilting angle of GM1 (Fig. 2(b), light grey). For the deFLiT configuration, the second galvo GM2 was synchronized and driven with counter-phasing signals with respect to GM1 (Fig. 2(b) dark grey, (c)), which allowed descanning the beam and maintaining a stationary non-tilted illumination at the center of the objective back aperture. Each GM unit was driven by a servo driver (MicroMax series 671; Cambridge Technology) controlled by a digital/analog converter board (PCI-6110; National Instrument). XYZ offsets of holographic spots coordinates caused by different off-axis holograms were calibrated and compensated. The control of the system was fully automatized through a homemade software written in Python 3 and using the open graphic library PyQt5 which allowed automatic calculation of the tiled holograms and synchronized control of the GM rotation and AOM attenuation. To measure the illumination at the OBA for deFLiT and FLiT, a CMOS camera (Thorlabs, DCC1545M) was placed at the OBA. The light intensity distribution used to illuminate the holograms was characterized in terms of horizontal and lateral widths, obtained from the gaussian fit of the vertical and horizontal cross sections using ImageJ.

2.2. Optical characterization of two-photon excitation

In order to optically characterize the spatial resolution and the intensity distribution of the holographic spots, 2PE fluorescence from a thin (~1 μm) spin-coated layer of rhodamine-6 G in polymethyl methacrylate 2% w/v in chloroform was induced by projection of holographic illumination patterns through the excitation objective (Olympus LUMPlanFL 40XW NA 0.8)

Biomedical Optics EXPRESS

and was collected through an opposite imaging objective (Olympus LUMPlanFL 60XW NA 0.9) in a transmission geometry on a sCMOS camera (pco, panda 4.2 bi). A short-pass filter was used to reject the laser light (Semrock, Brightline Multiphoton Filter 680/sp). 3D stacks were collected by maintaining the imaging objective in a fixed position and axially moving the excitation objective with 1 µm steps by means of a piezoelectric motor along the z-direction. The axial distribution of intensity on different spots was measured by integrating the pixel intensity across circular region of observations (ROIs) around the spots in each z plane. The intensity and axial resolution for each spot have been evaluated and reported as maximum intensity and Full Width Half Maximum (FWHM), respectively. Images have been analyzed with ImageJ and 3D rendering is performed with Imaris. To measure the tilt of the volumes of excitation enabled by different holograms φ_i, we computed for each hologram 2 axially-separated spots at the nominal coordinates (x,y,z) = (0,0,±50) µm. We then acquired the corresponding 3D stacks and we measured the angle θ_i between the objective optical axis and the line joining the center of the 2 spots.

2.3. Modeling of the impact of beam diaphragming on 2P excitation efficiency

The signal generated by a 2P excitation process can be expressed as $S_{2P} = \gamma P^2/f\tau$, where P is the averaged illumination power, τ is the laser pulse width, f is the laser repetition rate and γ is a multiplicative constant including the cross-section and the quantum yield of the excited molecule. To model how the generated S_{2P} signal was affected by beam diaphragming at the objective pupil plane for deFLiT illumination, we modeled the illumination shape at the OBA for each hologram with an elliptic gaussian light distribution of width W_x and W_y at position (x_i,y_i) in the x and y directions, respectively. Estimations for W_x and W_y, and (x_i,y_i) positions were directly obtained by fitting the X- and Y- experimental intensity profiles of the beams taken at the OBA with a CMOS camera with gaussian curves . The fraction of transmitted average power $P(\varphi_i)$ for each hologram position, was then estimated by considering the geometrical intersection between the elliptic beams corresponding to each hologram and the OBA. To estimate how the OBA affected the pulse durations $\tau(\varphi_i)$, we simulated for each hologram position the spatial chirp of the beam at the OBA using the spectral bandwidth of the laser ($\Delta\lambda = 12.5$ nm), the grating frequency and the optical path, and weighting the effect of the pupil cross-section on each spectral component. We then obtained the transmitted temporal pulse width $\tau(\varphi_i)$ at the sample through the Fourier transform of the resulting bandwidth. The resulting 2P signal produced by each hologram was then calculated using the expression: $S_{2P}(\varphi_i) = \gamma P(\varphi_i)^2/f\tau(\varphi_i)$. In particular, we considered two different OBA illuminations either given by an SLM-to-OBA magnification equal to 1 (as in the current FLiT setup) or 0.9 (as in the current deFLiT setup). This last case allowed a more accurate comparison of the expected performances of FLiT and deFLiT in the very same OBA illumination conditions.

3. Results

To compare the descanned configuration, deFLiT, with the previously presented FLiT configuration we first used a CMOS camera at the objective back aperture (OBA) plane to monitor the spatial distribution of the incoming beam plane while scanning the chirped excitation beam between the different holograms (Fig. 3) following the *descan* and the *scan* paths (Fig. 2(a), grey and blue areas).

We subdivided the SLM in 39 tiled holograms φ_i (Fig. 2(a), inset), vertically aligned in the direction orthogonal to the grating dispersion (y-direction). We used the galvanometric mirror GM1 to scan the spatially chirped beam onto the SLM between the different holograms (Fig 1(b)). In the FLiT configuration, the OBA and LC-SLM planes are directly conjugated (Fig. 3(a)) and the ellipsoidal chirped beam which scans the different holograms of the LC-SLM also vertically scans the OBA (Fig. 3(c),(e),(f)). Opposite to that, in deFLiT, a second galvo unit GM2

Biomedical Optics EXPRESS

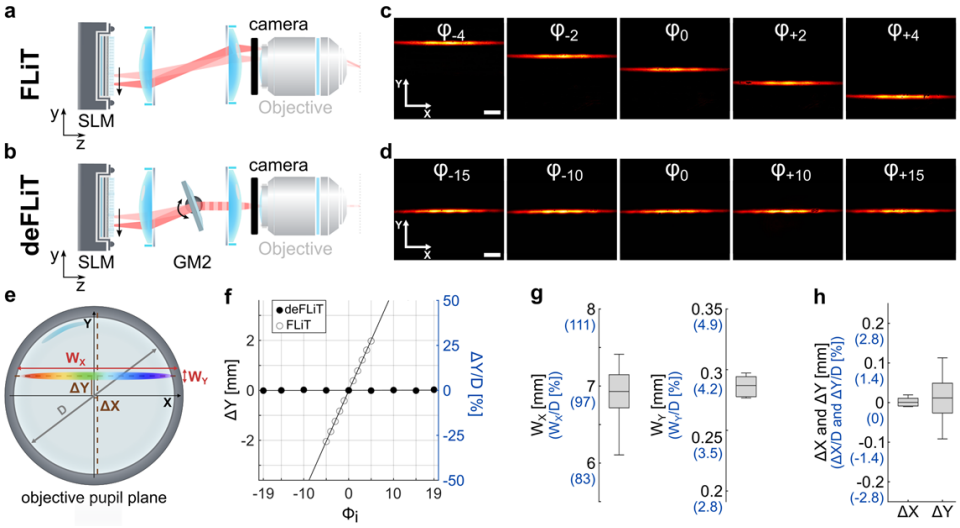

Fig. 3. Light distribution at the objective entrance with descanned-FLiT. (a),(b) Schematics of the detection scheme to image the incoming beam with a CMOS camera at the OBA for non-descanned FLiT (a) and descanned FLiT (b). **(c),(d)** XY intensity distribution of the beam at the OBA for different tiled holograms in FLiT (c) and deFLiT (d). The SLM was subdivided in 39 horizontal rectangular holograms φ_i (with $i = 0$ and $i = \pm 19$ the holograms in the middle and at the edges of the SLM, respectively). Scale bar 1 mm. **(e)** Schematics of a temporally-focused line beam at the OBA plane. W_X, W_Y and ΔX, ΔY represent the beam-waists and the beam-shifts in the x- and y-directions, respectively. y-direction orthogonal to the grating dispersion. D is the OBA diameter. **(f)** ΔY displacement of the beam for FLiT (empty circles) and deFLiT (filled circles) in mm (left, black y-axis) and as a percentage of the pupil diameter D (right, blue y-axis). Fittings are indicated with black lines. **(g),(h)** Variation of the beam-waists W_X and W_Y (g) and beam-shifts ΔX and ΔY (h) along the x- and y-directions at the OBA for different holograms in deFLiT, extracted from Gaussian fittings of the illumination profiles in (d). W_X, W_Y, ΔX and ΔY distributions are reported in mm (black y-axes) and as a percentage of the pupil diameter D (blue y-axes). Bars and middle horizontal lines indicate standard deviations and means.

counteracts the beam scanning from GM1 (Fig. 3(b)) maintaining the illumination beam in the middle of the OBA (Fig. 3(d),(f)). Importantly, we observed that during the descan process, the spatial distribution of the beams at the OBA was substantially unaltered, with an averaged beam waist among the different holograms of 0.29 ± 0.03 mm and 6.9 ± 0.4 mm (as mean ± st.dev., respectively in the x- and y- directions) (Fig. 3(g)). Also, spatial oscillations of the beam during descan were negligible, corresponding to spatial fluctuations around the OBA center as low as ±12 µm and ±91 µm in the x- and y-directions, equal to ±0.2% and ±1.3% of the pupil diameter (Fig. 3(h)).

Next, we analyzed the intensity distribution generated onto the sample by the different holograms in the two configurations as a function of the hologram position on the SLM. For this, we encoded each of the 39 tiled holograms to generate a single spot at the objective focal plane and measured the corresponding 2PE-fluorescence onto a thin layer of Rhodamine 6 G. We observed that the xy shape of the holographic spots was substantially unaltered in both cases (Fig. 4(a)). However, as expected, in the case of FLiT, the fluorescence intensity decreased as the position of the corresponding hologram imaged at the OBA moved away from the center, reaching nearly 50% of the 2P fluorescence intensity produced by the central hologram $\varphi_{0,}$ for

Biomedical Optics EXPRESS

the holograms φ_{-6} and φ_{+6} (corresponding to beam shifts of ±2.4 mm at the OBA, equivalent to ±33% of the OBA diameter), and dropping to zero (<3% of relative 2P fluorescence intensity) for holograms φ_{-10} and φ_{+8} (corresponding to beam shifts of -4.1 mm and +3.2 mm at the OBA, equivalent to -57% and 45% of the OBA diameter, respectively) (Fig. 4(b)). These results are in agreement with theoretical simulations of 2P intensity drops due to pupil diaphragming (Fig. 4(b), plain and dashed black curves and methods for modeling details). Conversely, the experimental deFLiT system enabled maintaining >75% of the 2P signal up to the φ_{-19} and φ_{+12} holograms (Fig. 4(b), black dots). Residual power losses for the most distal holograms were likely due to distortions or partial crops of the beam when travelling at very off-axis edges of the optics between GM1 and GM2.

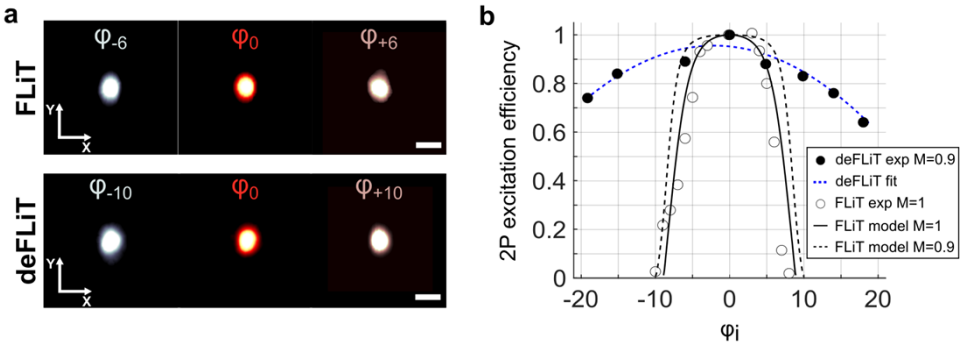

Fig. 4. In-focus holographic light-patterns. **(a)** Representative XY images of the 2P fluorescence induced by a single spot encoded by different tiled holograms (according to the hologram number indicated in the figure) for FLiT and deFLiT. Scale bar 10 µm. **(b)** Variation of the experimental 2P excitation intensity of a single spot encoded by different tiled holograms for FLiT (empty circles) and deFLiT (filled circles). Blue dashed line is a polynomial fit of the deFLiT experimental data. Black solid line indicates the expected variation given by the experimental beam geometry (details in methods) for the FLiT system. Black dashed line indicates the expected variation in a FLiT system by assuming equal SLM-to-OBA magnification for FLiT and deFLiT.

We then characterized, for the two cases, the capability to generate 3D patterns of spots. As previously reported [27], in FLiT, off-axis holograms at the OBA obliquely illuminated the sample which resulted in axially tilted spots and volumes of excitations (Fig. 5(a)). For holograms from φ_{-6} to φ_{+6}, we measured an axial tilt from -24° to +26° (Fig. 5(b)). This restricted the portion of excitation volume where the different holograms could overlap to a region of $120 \times 120 \times 100$ µm^3 (Fig. 5(c), white dashed rectangle). Opposite to that, for deFLiT, the scan of the 39 holograms at the SLM plane gave rise to a negligible optical axis tilt (0.3 ± 1.1°, as mean ± st.dev. spot axial tilt) (Fig. 5(a),(b)). Consequently, deFLiT provided on-axis colocalized excitation over $120 \times 120 \times 500$ µm^3 (Fig. 5(d)). Within this volume, we measured an axial resolution of 10 ± 2 µm in the perifocal region (assumed ± 50 µm from focal plane) and of up to 22 ± 7 µm in the distal portion of the volume (Fig. 5(e)), and the axial resolution was homogeneous among all holograms. The lateral spot sizes were 6.5 ± 0.7 µm and 8.7 ± 1.3 µm along the x- and y-direction, respectively, and were homogenous along the z-axis and among holograms (Fig. 5(e)). Consistently with previous findings for conventional holography [22], fluorescence variation within the excitation volume from different spots was below 45% (st.dev.), and was homogenous across different holograms (Fig. 5(f)). We finally assessed the deFLiT light-targeting accuracy among holograms generated within this volume by encoding the same 3D patterns to different tiled holograms. We obtained an average targeting accuracy below 18% of the spot extension (Fig. 5(g)), which indicates that minor excitation variabilities are expected when sweeping between holograms.

Biomedical Optics EXPRESS

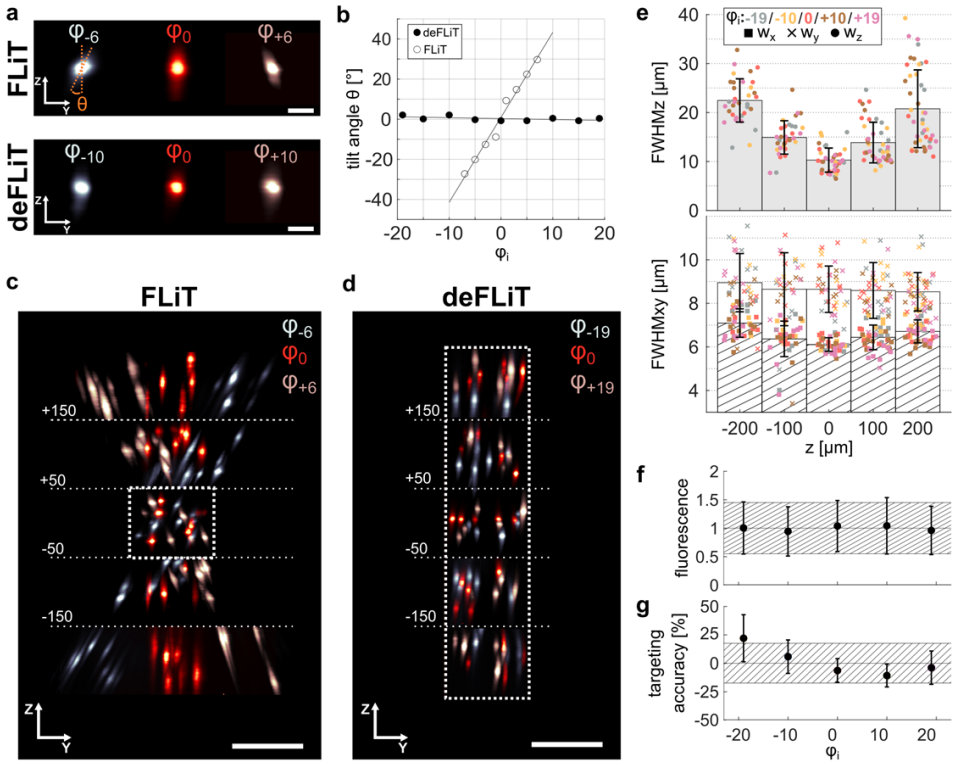

Fig. 5. Volumetric distribution of multi-spots holographic light-patterns. **(a)** YZ intensity projection of spots generated in the center of the field of excitation by different tiled holograms (according to the hologram number indicated in the figure) for FLiT and deFLiT, respectively. Scale bar 10 µm. **(b)** Angle θ between the optical axis and the tilted axial axis of the holographic spot in the center of the FOE as in (a) for different tiled holograms, in FLiT (empty circles) and deFLiT (filled circles). **(c),(d)** YZ intensity distributions of 3D randomly distributed spots generated by different tiled holograms for FLiT (c) and deFLiT (d) over an axial range of 500 µm. Scale bar 100 µm. Different colors correspond to different tiled holograms. **(e)** Axial (top) and lateral (bottom) FWHMs of the intensity profiles of spots randomly generated in 3D, for deFLiT as in (d), against their axial position. Each marker represents one spot. Different colors indicate spots encoded by different tiled holograms. Bars indicate the mean values in 100 µm range around the designated z position. Vertical lines indicate st. dev. (n = 194 spots). **(f)** 2PE fluorescence of 3D random spots in deFLiT mode as in (d) obtained with different holograms. The dots and the error bars represent the mean and std per hologram, respectively. The black horizontal line and dashed area represent the global mean and std. (n = 194 spots). **(g)** Spot targeting accuracy when targeting n = 45 spot locations, randomly distributed across a $120 \times 120 \times 500$ µm^3 in deFLiT mode, with different tiled holograms. For each spot location, spot targeting accuracy of hologram φ_i is defined as the distance between the experimentally reached position using hologram φ_i and the barycenter of the positions reached with holograms φ_{-19}, φ_{-10}, φ_0, φ_{+10} and φ_{+19} for this spot, divided by the mean spot size. Dots and error bars represent the mean and std per hologram, respectively. The black horizontal lines and dashed area represent the global mean and std. (n = 45 per hologram φ_i).

Biomedical Optics EXPRESS

4. Discussion

We have developed and characterized a descanned variant, named deFLiT, of a previously reported optical scheme for ultra-fast sequential light targeting (FLiT) based on the rapid switching of a temporally focused beam between H vertically aligned holograms on a SLM at kHz rates. We demonstrated that FLiT enables an ultra-fast sequential stimulation of $(H + 1)/2$ distinct targets and, using cyclic illumination, multi-target optogenetic activation with $\sqrt{H}$- to H- times reduced power with respect to conventional holography [27].

In the original FLiT configuration, a relay telescope is used to directly image the SLM display onto the OBA. Off-centered holograms tiled on the SLM are thus relayed off-axis at the OBA, which then leads to axial tilts of the holographic illumination onto the sample. Also, off-centered holograms are partly cropped at the sides, which leads to a proportional intensity cut of the corresponding generated patterns. Minimizing these effects requires maximizing the number of holograms projected into the middle region of the objective pupil. This can be achieved by reducing the magnification between the SLM and the OBA and so by underfilling the OBA. This however also reduces the effective objective NA, and therefore enlarges the axial resolution. Alternatively, each hologram on the SLM can be narrowed by reducing the number of pixels per hologram in the y-direction so to increase the hologram number in the central OBA region. This however also reduces the amount of encodable information per hologram [29] and limits the maximum deliverable power per hologram (limited by the SLM damage threshold). For example, in a previously demonstrated configuration for FLiT, a trade-off between axial resolution, excitation volume (FOE), number of illuminated holograms (H), and power losses below 33% was reached [27] by using a small pixel pitch (12.5 µm) SLM tiled in 45 holograms, a large aperture objective (20x magnification, 1.0 NA) and the 23 central holograms (corresponding to 51% of the total SLM vertical size).

In the present manuscript, we propose an alternative optical design, deFLiT, where a second scanning unit enables to project the illuminated hologram always at the center of the OBA independently of the position of the illuminated hologram on the SLM. We demonstrate that by using a conventional large pixel size-SLM (20 µm) and a 40x, 0.8 NA objective we could use 100% of the SLM (divided in 39 holograms) with power losses below 18%, and an on-axis colocalized excitation volume, FOE, of $120 \times 120 \times 500$ µm^3. For comparison, maintaining the power losses below 18% with a non-descanned-FLiT system using the same SLM divided in 39 holograms, same objective and same SLM-to-objective magnification, would limit to use only the 12 most central holograms (i.e., only 31% of the SLM vertical size) and would reach tilted excitation volumes.

While deFLiT refines the performances of FLiT for any SLM/objective system, deFLiT presents the disadvantage of a more complex optical system and thus also a more complex alignment. In particular, the holographic pattern generated in the Fourier plane after the SLM must be de-magnified to fit on the descan mirrors. In the present design, 3mm-size descan mirrors are used for maximal speed, therefore a 4-lenses telescope is needed to fit the holographic FOE on them, which introduces power losses and aberrations for beams travelling at very off-axis edges of the optics between GM1 and GM2. These undesirable effects could be mitigated by using larger galvanometric mirrors although in this case longer response times are expected. Alternative designs featuring different scan units could also be considered. These include polygonal scanning mirrors [30], acousto-optic deflectors [31] or rotating phase masks - that could encode prism-like phase modulation to tilt the beam in a transmission geometry.

In conclusion, we demonstrated deFLiT as an alternative design to FLiT, enabling to maximize the performances of FLiT in terms of number of usable holograms and reachable excitation volume. This configuration is especially indicated for configurations using high-magnification objectives and/or conventional large pixel (20 µm) SLMs.

Biomedical Optics EXPRESS

Funding. IHU FOReSIGHT (P-ALLOP3-IHU-000); Conseil Régional, Île-de-France (WASCO DIM-Elicit); National Institutes of Health (1RF1NS128772-01); HORIZON EUROPE European Research Council (DEEPER, 101016787); European Research Council (Holovis ERC2019-ADG-885090).

Acknowledgments. We thank Clément Molinier for the development of the software for phase masks generation and SLM control and Christophe Tourain for technical support on the electronics.

Disclosures. The authors declare that there are no conflicts of interest related to this article.

Data availability. Data underlying the results presented in this paper are not publicly available at this time but may be obtained from the authors upon reasonable request.

References

1. O. Yizhar, L. E. Fenno, T. J. Davidson, M. Mogri, and K. Deisseroth, "Optogenetics in neural systems," Neuron **71**(1), 9–34 (2011).
2. L. Fenno, O. Yizhar, and K. Deisseroth, "The Development and Application of Optogenetics," Annu. Rev. Neurosci. **34**(1), 389–412 (2011).
3. F. Schneider, C. Grimm, and P. Hegemann, "Biophysics of Channelrhodopsin," Annu. Rev. Biophys. **44**(1), 167–186 (2015).
4. E. Ronzitti, C. Ventalon, M. Canepari, B. C. Forget, E. Papagiakoumou, and V. Emiliani, "Recent advances in patterned photostimulation for optogenetics," J. Opt. **19**(11), 113001 (2017).
5. E. Ronzitti, V. Emiliani, and E. Papagiakoumou, "Methods for Three-Dimensional All-Optical Manipulation of Neural Circuits," Front. Cell. Neurosci. **12**, 469 (2018).
6. A. M. Packer, B. Roska, and M. Häusser, "Targeting neurons and photons for optogenetics," Nat. Neurosci. **16**(7), 805–815 (2013).
7. H. Adesnik and L. Abdeladim, "Probing neural codes with two-photon holographic optogenetics," Nat. Neurosci. **24**(10), 1356–1366 (2021).
8. A. M. Packer, D. S. Peterka, J. J. Hirtz, R. Prakash, K. Deisseroth, R. Yuste, O. Yizhar, B. Grewe, C. Ramakrishnan, N. Wang, I. Goshen, A. M. Packer, D. S. Peterka, R. Yuste, M. J. Schnitzer, and K. Deisseroth, "Two-photon optogenetics of dendritic spines and neural circuits," Nat. Methods **9**(12), 1202–1205 (2012).
9. J. P. Rickgauer, K. Deisseroth, and D. W. Tank, "Simultaneous cellular-resolution optical perturbation and imaging of place cell firing fields," Nat. Neurosci. **17**(12), 1816–1824 (2014).
10. E. Papagiakoumou, F. Anselmi, A. Bègue, V. de Sars, J. Glückstad, E. Y. Isacoff, and V. Emiliani, "Scanless two-photon excitation of channelrhodopsin-2," Nat. Methods **7**(10), 848–854 (2010).
11. A. R. Mardinly, I. A. Oldenburg, N. C. Pégard, S. Sridharan, E. H. Lyall, K. Chesnov, S. G. Brohawn, L. Waller, and H. Adesnik, "Precise multimodal optical control of neural ensemble activity," Nat. Neurosci. **21**(6), 881–893 (2018).
12. I.-W. Chen, E. Ronzitti, B. R. Lee, T. L. Daigle, D. Dalkara, H. Zeng, V. Emiliani, and E. Papagiakoumou, "In vivo sub-millisecond two-photon optogenetics with temporally focused patterned light," J. Neurosci. **39**(18), 1785-18 (2019).
13. G. L. B. Spampinato, E. Ronzitti, V. Zampini, U. Ferrari, F. Trapani, H. Khabou, A. Agraval, D. Dalkara, S. Picaud, E. Papagiakoumou, O. Marre, and V. Emiliani, "All-optical inter-layers functional connectivity investigation in the mouse retina," Cells Rep. Methods **2**(8), 100268 (2022).
14. J. H. Marshel, Y. S. Kim, T. A. Machado, S. Quirin, B. Benson, J. Kadmon, C. Raja, A. Chibukhchyan, C. Ramakrishnan, M. Inoue, J. C. Shane, D. J. McKnight, S. Yoshizawa, H. E. Kato, S. Ganguli, and K. Deisseroth, "Cortical layer–specific critical dynamics triggering perception," Science **365**(6453), eaaw5202 (2019).
15. L. Carrillo-Reid, S. Han, W. Yang, A. Akrouh, and R. Yuste, "Controlling Visually Guided Behavior by Holographic Recalling of Cortical Ensembles," Cell **178**(2), 447–457.e5 (2019).
16. M. dal Maschio, J. C. Donovan, T. O. Helmbrecht, and H. Baier, "Linking Neurons to Network Function and Behavior by Two-Photon Holographic Optogenetics and Volumetric Imaging," Neuron **94**(4), 774–789.e5 (2017).
17. J. V. Gill, G. M. Lerman, H. Zhao, B. J. Stetler, D. Rinberg, and S. Shoham, "Precise Holographic Manipulation of Olfactory Circuits Reveals Coding Features Determining Perceptual Detection," Neuron **108**(2), 382–393.e5 (2020).
18. C. Lutz, T. T. S. Otis, V. DeSars, S. Charpak, D. a DiGregorio, and V. Emiliani, "Holographic photolysis of caged neurotransmitters," Nat. Methods **5**(9), 821–827 (2008).
19. J. P. Rickgauer and D. W. Tank, "Two-photon excitation of channelrhodopsin-2 at saturation," Proc. Natl. Acad. Sci. U. S. A. **106**(35), 15025–15030 (2009).
20. R. Prakash, O. Yizhar, B. Grewe, C. Ramakrishnan, N. Wang, I. Goshen, A. M. Packer, D. S. Peterka, R. Yuste, M. J. Schnitzer, and K. Deisseroth, "Two-photon optogenetic toolbox for fast inhibition, excitation and bistable modulation," Nat. Methods **9**(12), 1171–1179 (2012).
21. E. Ronzitti, R. Conti, V. Zampini, D. Tanese, A. J. Foust, N. Klapoetke, E. S. Boyden, E. Papagiakoumou, and V. Emiliani, "Sub-millisecond optogenetic control of neuronal firing with two-photon holographic photoactivation of Chronos," J. Neurosci. **37**(44), 10679–10689 (2017).
22. N. Accanto, C. Molinier, D. Tanese, E. Ronzitti, Z. L. Newman, C. Wyart, E. Isacoff, E. Papagiakoumou, and V. Emiliani, "Multiplexed temporally focused light shaping for high-resolution multi-cell targeting," Optica **5**(11), 1478 (2018).

Biomedical Optics EXPRESS

23. N. M. Pegard, A. R. Marinly, A. Oldenburg, S. Sridharan, L. Waller, and H. Adesnik, "Three-dimensional scanless holographic optogenetics with temporal focusing (3D-SHOT)," Nat. Commun. **8**(1), 1228 (2017).
24. B. Sun, P. S. Salter, C. Roider, A. Jesacher, J. Strauss, J. Heberle, M. Schmidt, and M. J. Booth, "Four-dimensional light shaping: manipulating ultrafast spatiotemporal foci in space and time," Light: Sci. Appl. **7**(1), 17117 (2017).
25. D. Oron, E. Tal, and Y. Silberberg, "Scanningless depth-resolved microscopy," Opt. Express **13**(5), 1468–1476 (2005).
26. E. Papagiakoumou, V. de Sars, D. Oron, and V. Emiliani, "Patterned two-photon illumination by spatiotemporal shaping of ultrashort pulses," Opt. Express **16**(26), 22039 (2008).
27. G. Faini, D. Tanese, C. Molinier, C. Telliez, M. Hamdani, F. Blot, C. Tourain, V. de Sars, F. Del Bene, B. C. Forget, E. Ronzitti, and V. Emiliani, "Ultrafast light targeting for high-throughput precise control of neuronal networks," Nat. Commun. **14**(1), 1888 (2023).
28. R. Di Leonardo, F. Ianni, and G. Ruocco, "Computer generation of optimal holograms for optical trap arrays," Opt. Express **15**(4), 1913 (2007).
29. O. Hernandez, E. Papagiakoumou, D. Tanese, K. Fidelin, C. Wyart, V. Emiliani, D. Tanesee, K. Felin, C. Wyart, and V. Emiliani, "Three-dimensional spatiotemporal focusing of holographic patterns," Nat. Commun. **7**(1), 11928 (2016).
30. S. Choi, P. Kim, R. Boutilier, M. Y. Kim, Y. J. Lee, and H. Lee, "Development of a high speed laser scanning confocal microscope with an acquisition rate up to 200 frames per second," Opt. Express **21**(20), 23611 (2013).
31. V. Iyer, T. M. Hoogland, and P. Saggau, "Fast Functional Imaging of Single Neurons Using Random-Access Multiphoton (RAMP) Microscopy," J. Neurophysiol. **95**(1), 535–545 (2006).